

Received April 9, 2019, accepted April 27, 2019, date of publication May 6, 2019, date of current version May 17, 2019.

Digital Object Identifier 10.1109/ACCESS.2019.2914766

# A Recognition Technology of Transmission Lines Conductor Break and Surface Damage Based on Aerial Image

YE ZHANG<sup>1,2</sup>, XINBO HUANG<sup>1,2</sup>, (Senior Member, IEEE), JIANYUAN JIA<sup>1</sup>, AND XINHUI LIU<sup>3</sup>

<sup>1</sup>School of Mechano-Electronic Engineering, Xidian University, Xi'an 710071, China

<sup>2</sup>School of Electronics and Information, Xi'an Polytechnic University, Xi'an 710048, China

<sup>3</sup>School of Electronic and Information Engineering, Xi'an Jiaotong University, Xi'an 710049, China

Corresponding author: Xinbo Huang (huangxb1975@163.com)

This work was supported in part by the National Natural Science Foundation of China under Grant 51177115, in part by the Key Technology Innovation Team Project of Shaanxi Province under Grant 2014KCT-16, and in part by the Key Research and Development Program of Shaanxi Province under Grant 2018ZDXM-GY-040.

**ABSTRACT** The aluminum strands break and surface damage will gradually develop into irreversible destruction to the conductors and the whole transmission lines, and even lead to serious power outages. In order to find out the potential strands break and damage faults and prevent its further deterioration, a recognition method of conductor break and surface defects in transmission lines' unmanned aerial vehicle (UAV) inspection is presented in this paper. First, a conductor image is obtained by the UAV image acquisition system, and then, the conductor region is extracted by the adaptive threshold segmentation after the enhancement processing by the gray variance normalization method (GVN). Second, the conductor break is detected by the square wave transformation (SWT) of its grayscale distribution curves, which is simple and effective. Meanwhile, the conductor surface defects are identified by the projection algorithm of the GVN image of the conductor region. Finally, calculating the number of broken strands and filtering the suspect defects, the final fault diagnosis results can be obtained. We analyze the performance of the technology by a series of experiments, and the results demonstrate that the proposed method can measure the conductor break and surface defects faults with the average accuracy of 90.45% and 92.05%, respectively. The health condition of the conductor can be monitored based on the method presented in this paper, by which the safe operation of transmission lines can be guaranteed.

**INDEX TERMS** Conductor break, surface defects, image processing, transmission lines, UAV inspection.

## I. INTRODUCTION

As an important component of high-voltage transmission lines, aluminum conductors steel-reinforced (ACSR) plays the dual role of electric power delivery and mechanical strength during operation. Due to long-term exposure to the field environment, affected by wind vibration, galloping of iced conductor, environmental erosion, etc., aluminum strands are prone to various types of damage, from surface damage to partial break and then develop into fracture of the whole ACSR. When the aluminum strands are damaged, the load-bearing capacity is reduced, and the risk of conductor fracture increases, which poses a potential risk to the

The associate editor coordinating the review of this manuscript and approving it for publication was Ke Gu.

conductors, power transmission and transformation equipment and personal safety [1]–[3].

In order to effectively improve the operating efficiency of transmission lines and reduce the frequency of failures, researchers in Russia, Canada, Japan, India, Norway, Finland and other countries with frequent failures in transmission lines have carried out a lot of research on the component materials, the failure mechanism and the running status of the transmission conductors. And some preliminary research results have been obtained, such as the improvement of the constituent materials of the transmission wire, the microscopic change process of the wire surface damage, and the fault detection of the wire breakage [4]–[8]. These methods are preventive mostly on the materials and mechanism, and the existing break and damage problem of the in-operation

conductors is mainly observed by manual detection which is time consuming, low accurate and poorly secure.

In recent years, the unmanned aerial vehicle (UAV) inspection technology has been developed in transmission lines with the great progress of the aerial image sensors and computer vision techniques [9]–[12]. Some researchers have put forward different kinds of algorithms for power lines detection and extraction in aerial images [13]–[16]. Some others are focus on the segmentation and fault detection algorithm for aerial insulator images [17]–[21] and also the detection of bird’s nest in high power lines [22]. The vision-based technology has also been used in defect detection of the weld bead and of rail heads, and in the measurement of the lay length of metallic conductor [23]–[25]. However, due to the complex formative factors, the diverse manifestation, and the limitations of images acquisition, there were no available methods based on vision about how to timely monitor the conductor break and defects.

In this paper, we present a measurement method of break and defects on transmission conductors based on aerial image sensors in the unmanned aerial vehicle (UAV) inspection, which can obtain the break and defects on the transmission conductors in operation by using an aerial vision system and the image processing algorithms. The vision system acquires several views of transmission conductor pictures that are employed to extract the conductor region. By analyzing the gray value distribution of the conductor region, it is possible to measure the conductor break with the proposed Z-shaped waveforms model, and to detect the surface defects by the projection algorithm of the conductor region. The presented method provides a new method for monitoring the break and defects of transmission conductors in operation.

This paper is organized as shown in Fig. 1. In Section II, we describe the overview of a measurement technology of transmission lines conductor break and surface defects based on aerial image sensors. Section III proposes the analysis algorithms of conductor break and defects recognition in separate. Section IV gives the field experimental results and analysis of the proposed algorithms. Section V provides the conclusions and suggests the possible future investigation.

## **II. OVERVIEW OF A MEASUREMENT TECHNOLOGY OF TRANSMISSION LINES CONDUCTOR BREAK AND DEFECTS BASED ON AERIAL IMAGE SENSORS**

The online technology for measuring conductor break and surface defects based on aerial vision sensors proposed in this paper consists of three parts: the online monitoring device based on aerial vision sensors [28], [29] and the unmanned aerial vehicle (UAV), the 4G communication network, and the monitoring center with the conductor break and defects analysis software installed. In our UAV patrol inspection system, a high definition digital camera, which is installed on the UAV, is used to capture images of transmission conductors as the UAV moves over the transmission lines, and then, the

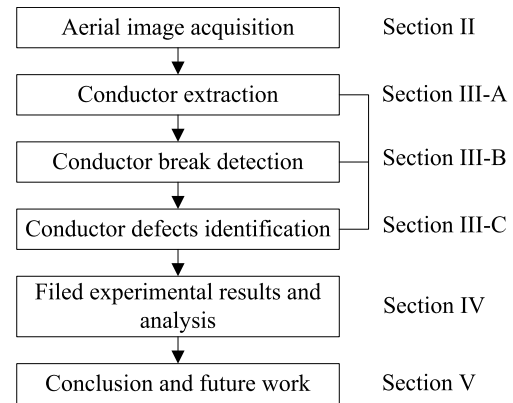


**FIGURE 1.** Flowchart of the measurement technology of transmission lines conductor break and defects based on aerial image sensors.

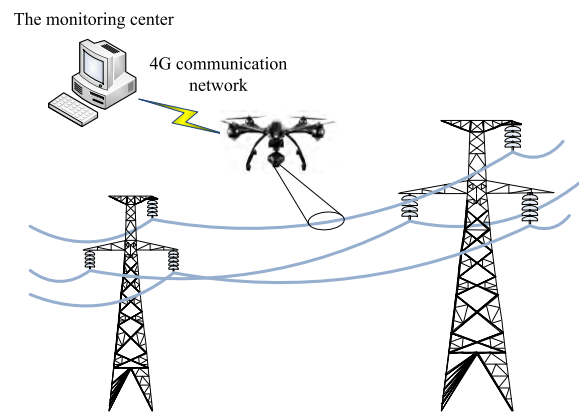


**FIGURE 2.** Block diagram of the online monitoring system for conductor break and defects based on aerial vision sensors and UAV.

obtained images are decompressed and sent to the monitoring center by 4G communication networks. Then the conductor break and defects are analyzed automatically using a conductor break and defects analysis software which has embedded the proposed corresponding algorithms. UAV patrol inspection is not only low-cost but also has the advantages of high efficiency, low risk, and appealing performance and is regarded as the most attractive technique for transmission lines inspection. This paper focuses on the core techniques of UAV patrol inspection system. The block diagram of the proposed technology is shown in Fig. 2.

#### **A. ONLINE IMAGE ACQUISITION DEVICE BASED ON AERIAL VISION SENSORS AND UAV**

The online image acquisition device is made up of several available components. The basic component is a DJI JY-UAV-10 UAV, which carries a digital camera with a resolution of 12million pixels and a shutter speed of 8-1/8000 seconds. A 4G communication model is utilized to transmit conductor images to the ground monitoring center, and to receive the commands from the monitoring center such as time set, sampling interval, real-time sampling and even initialization of the aerial image acquisition sensor [30], [31].

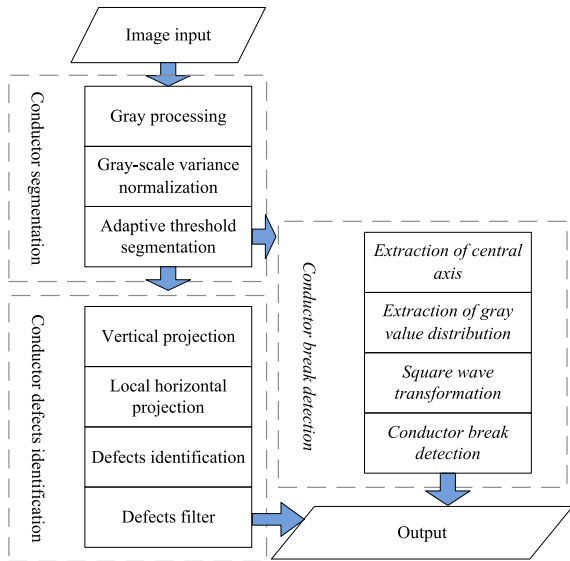


**FIGURE 3.** Block diagram of image analysis algorithm for conductor break and defects.

## B. MONITORING CENTER

The monitoring center consists of a computer, a video server and a database server [32]. The image receiving and decompression software and the conductor break and defects analysis software are installed in the computer. After a conductor image is generated by the image receiving and decompression software, it is processed by the conductor break and defects analysis software, which aims to efficiently detect possible break and defects in the image. The analysis software was developed combining VC++ [33] and HALCON [34]. The main functions include real-time image importing, algorithm analysis, fault diagnosis, alarm transmission, image display and defect information display [35], [36]. The special database was created in Oracle 11g. The conductor breaks and defects analysis algorithms will be presented in Section III, by which the conductor breaks and defects will be measured.

## III. ANALYSIS ALGORITHMS FOR THE RECOGNITION OF CONDUCTOR BREAK AND SURFACE DEFECTS

The image analysis algorithm module includes three main modules: conductor extraction, conductor break detection, and conductor surface defects identification. Fig. 3 shows the diagram of the algorithm flow.

- **Conductor extraction:** A transmission line image obtained by the image acquisition device includes not only the conductor region, but also the interference background. Therefore, the region of the conductor should be first extracted in order to reduce the area to be inspected in the subsequent procedures. We put forward the algorithm called the gray-scale variance normalization (GVN). GVN is supported by the observations: 1) conductor regions have similar gray value, and 2) conductor regions have higher definition in aerial images compared with background areas. More details about this algorithm are seen in the A part of Section III.

- **Conductor break detection:** Since the gray distribution of the external aluminum strands of the unbroken conductor showing a good periodicity on the transverse axis, if there are some regions break the periodicity, then they can be initially judged as the potential conductor break region, so gray scale distribution is a vital characteristic to distinguish break region from the undamaged area. We propose the square wave transformation (SWT) method to represent the gray scale distribution of the external aluminum strands. A square waveform with too large or too small periods can be considered as suspect conductor break region. Then the number of broken aluminum strands is simply obtained by dividing the width of suspect conductor break regions by the actual width of a single aluminum strand. The conductor break detection algorithm is presented in the B part of Section III.

- **Conductor surface defects identification:** In the GVN image of the conductor region, the defects on the conductor region are brighter than other areas and are clustered together. Taking the gray value distribution and location distribution into account, we put forward the defects identification algorithm based on the projection of the GVN image of conductor region, which is called PGVN [25]–[27]. In PGVN algorithm, the suspect positions of defects on the horizontal direction of the conductor are first located by analyzing the vertical projection of the normalized gray-scale variance value of each column. After the vertical projection is processed by a high-pass filtering rule, each suspect peaks of the vertical projection profile determines a subimage. Then, the vertical suspect defects regions are obtained based on the horizontal projection of the subimage. Finally, each pair of suspect peaks in the horizontal and vertical projection profiles forms a suspect rectangle, and each rectangle is identified as a defect. PGVN is not only fast but also robust to noise. PGVN is described in the C part of Section III.

## A. CONDUCTOR EXTRACTION

Most of the aerial transmission line images are color (RGB) images. In order to reduce the amount of data to be processed, and to enhance the operation efficiency as well as to highlight the conductor region, the color model conversion or grayscale processing on the aerial images is required. The surface color of conductor region in the aerial images is prone to be gray and dim because the online image acquisition device suffers from the influence of natural light. Furthermore, the aerial images have the characteristic that the sharpness of the conductor region is higher than the trees, the buildings, and the roads in the background, that is, the gray value of the conductor is highly dispersed. In the conventional method, the essence of graying the target image is to process the gray value of each pixel, but it is found that the accuracy of the processing results is extremely degraded if we processed the aerial transmission line images through pixel-by-pixel. Based on these considerations, we propose the GVN to perform

grayscale processing of aerial images. The GVN method transforms the traditional ideal of directly processing the gray value of each pixel into the processing of the dispersion degree of pixel gray values. The specific calculation steps of the GVN are given by

$$\bar{Q} = \frac{1}{9} \sum_{i=1}^9 (Q_i) \quad (1)$$

where  $\bar{Q}$  is the mean gray value of each pixel in the template and  $Q_i$  represents the gray value of the  $i$ th pixel of the template, and then the variance of gray-scale value in every processing unit can be calculated according to (2)

$$q_5 = \frac{1}{9} \sum_{i=1}^9 (Q_i - \bar{Q})^2 \quad (2)$$

where  $q_5$  is the gray-scale variance of the center pixel with shaded color in a template. Traversing the entire image with the 3\*3 template in Fig. 4(a), the complete gray-scale variance map corresponding to the original image can be obtained. Furthermore, the gray-scale variance of each pixel is normalized by

$$m_{(x,y)} = \frac{q_{(x,y)} - q_{\min}}{q_{\max} - q_{\min}} \quad (3)$$

where  $m_{(x,y)}$  is the normalized gray value at the coordinate  $(x, y)$ ,  $q_{\max}$  is the maximum gray value in the gray-scale variance map while  $q_{\min}$  is the minimum gray value, and  $q_{(x,y)}$  is the gray value at coordinate  $(x, y)$  in the gray-scale variance map.

The comparison of the GVN method and other gray processing methods is shown in Table 1. The background purity

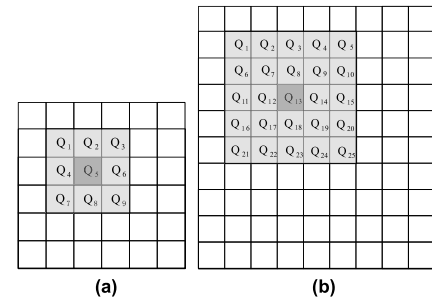


**FIGURE 4.** Schematic diagram of traversing convolution template. (a) 3\*3. (b) 5\*5.

and contrast of the GVN algorithm is higher, the target is clearer and the robustness is better. The weighted average graying method only realizes the basic grayscale processing; the saturation component can only highlights the conductor region when the background is quite different from the conductor, but the robustness is poor under some similar gray background. The histogram equalization method is better than the weighted average graying method and the saturation component, but it does not effectively suppress the background interference, which brings great challenges to the subsequent segmentation. In contrast, the proposed GVN method in this paper has the advantages of high anti-background interference, clarity and contrast. It also effectively promotes the subsequent image segmentation at the same time, which has certain advantages.

The segmentation of the conductor region is based on the GVN results. We adopting the common adaptive threshold segmentation combine with the morphological processing to carry out the conductor segmentation. Compared with the segmentation based on the common gray processing or

**TABLE 1.** Comparison of different image gray processing methods.

Number	1	2	3	4	5	6	7
Original image							
Weighted average graying							
Saturation							
Histogram equalization							
GVN method							

**TABLE 2.** Image segmentation.

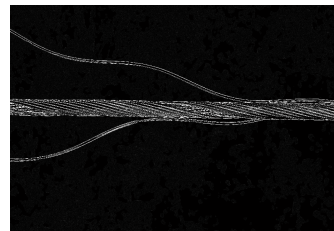
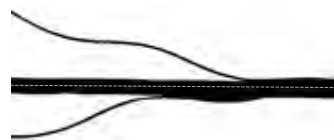
Number	Image	Gray image segmentation	GVN image segmentation
1			
2			
3			
4			
5			
6			
7			
8			

enhancement image, our method obtains better results for segmentation of the conductor region.

The segmentation of eight images under different conditions is shown in Table 2. The segmentation results based on the grayscale or enhancement processed images are shown in the third column, which still have some background noises or some holes inside, and some segmentation results are incomplete. On the other hand, the segmentation effects of eight images based on the GVN images are all ideal, which can effectively avoid the influence of external factors.

## B. CONDUCTOR BREAK DETECTION

After the segmentation of conductor region, we can focus on analyzing the conductor region without background interference. The extracted conductor region needs to be mapped back to its GVN image, because the gray value distribution on the GVN image of conductor region is essential parameter in the conductor break detection algorithm. In this section, we thoroughly analyze the conductor break detection algorithm by taking the image in Fig. 5 as an example.

**FIGURE 5.** GVN image of the conductor region.**FIGURE 6.** Extraction of the central axis of the conductor.

As for the conductor break detection algorithm, there are three important procedures: extraction of gray value distribution, square wave transformation (SWT) and broken strands identification. Gray value distribution of the external aluminum strands directly reflects the surface integrity of the conductor, and SWT highlights the periodicity of its gray value distribution. Eventually, the broken strands situation of transmission conductor is simply obtained by analyzing the width of each acquired Z-shaped waveform.

### 1) EXTRACTION OF GRAY VALUE DISTRIBUTION

As shown in Fig. 5, the surface of every aluminum strand has a higher gray value than the marginal gaps among each other, and the external aluminum strands have cyclic characteristics in structure, so that the gray scale distribution of unbroken conductor surface presents a cyclical cycle characteristic. Since the aluminum strands in different layer are wound in opposite directions and the winding angle is different, once it happens to the conductor break, it not only causes the broken aluminum strand upwarps or separates itself from the conductor, but also is accompanied by the barenness of the inner aluminum strands. This phenomenon will lead to the changes on the transverse spacing of external aluminum strands, and because of the lower gray value of the bared inner aluminum strands at the broken area, it will further destroy the original gray value periodicity characteristic.

Based on these observations and considerations, we transform the conductor break detection into the periodic detection of the gray value distribution on the conductor surface. First, the central axis of the conductor region is fitted by the least square fitting (LSF) method [35]. The fitting result is shown in Fig. 6.

Since the broken aluminum strand is not completely scattered from the conductor, it is not sufficient to detect the broken aluminum strands only on the central axis. Thereby, we first obtain the number of pixels occupied by the diameter of the conductor, and then we extract the gray value distribution on the axes at the 1/4, 1/2 and 3/4 thickness of the

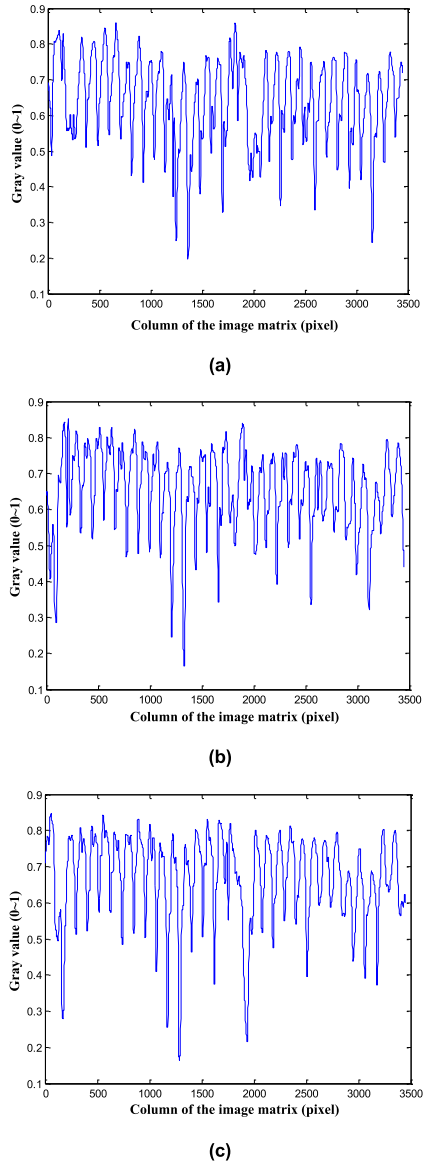


**FIGURE 7.** Gray value distribution on each axis of the broken conductor. (a) Axis at 1/4 thickness. (b) Central axis. (c) Axis at 3/4 thickness.

conductor separately. Because the transmission conductor is exposed all the year round, some low gray value points often appear in the high gray area on the conductor surface affected by various kinds of noise. This will affect the accurate extraction of cyclic gray value distribution and lead to a false detection of broken strands. Therefore, the median filtering processing is needed while extracting the gray value distribution on each axis [37], and the final results is as shown in Fig. 7.

## 2) SQUARE WAVE TRANSFORMATION (SWT)

Since the gray value distribution on each axis has certain randomness within a certain range of gray values, the acquired waveform has a quasi-periodic property, but there is no accurate cycle. For this reason, the square wave

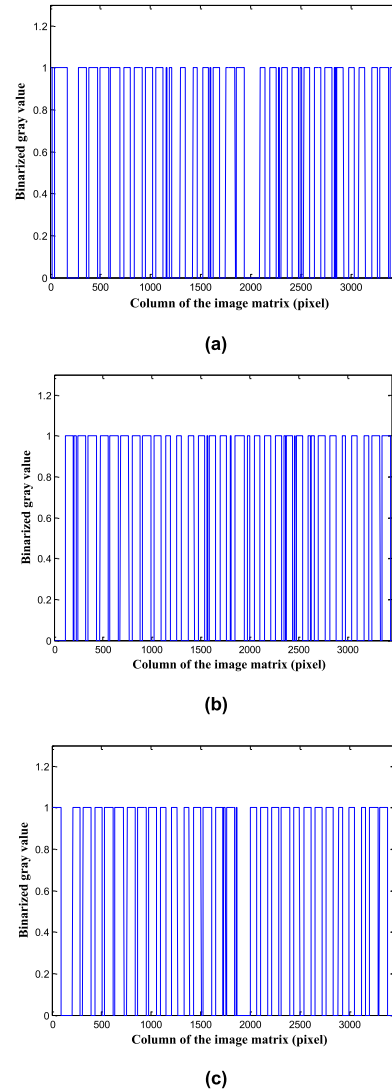


**FIGURE 8.** Square wave representation of gray scale distribution map. (a) Axis at 1/4 thickness. (b) Central axis. (c) Axis at 3/4 thickness.

transformation (SWT) method is proposed to better represent the cyclic characteristic of the gray value distribution. In this method, it employed a threshold to perform the binarization processing to the obtained waveforms in Fig. 7 so as to realize a square wave transformation. And the mean value  $(n_{\max} + n_{\min})/2$  of the maximum gray value and the minimum gray value is set as the binarization threshold, as a whole, the obtained waveforms in Fig. 7 is processed by the following rule.

$$p = \begin{cases} 0, & n \leq \frac{n_{\max} + n_{\min}}{2} \\ 1, & n > \frac{n_{\max} + n_{\min}}{2} \end{cases} \quad (4)$$

where  $n$  represents the gray value of any point on the obtained waveforms in Fig. 7,  $n_{\max}$  is the maximum gray value,  $n_{\min}$  is the minimum gray value, and  $p$  denotes the result of the binarization processing, and the obtained square waveforms are as shown in Fig. 8, where the width of a single Z-shaped

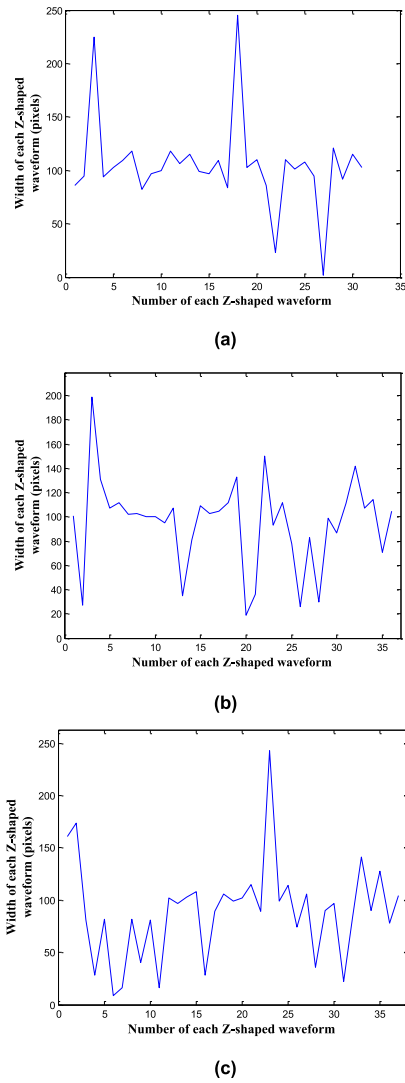


**FIGURE 9.** Width statistical graph of each Z-shaped waveform. (a) Axis at 1/4 thickness. (b) Central axis. (c) Axis at 3/4 thickness.

waveform can be used to characterize the width of the single aluminum strand.

### 3) IDENTIFICATION OF BROKEN STRANDS

To clearly characterize the width variation of each Z-shaped waveform, it is necessary to make a statistical analysis of the width  $P$  of each Z-shaped waveform. The statistical result on each axis is shown in Fig. 9.

As shown in Fig. 9, the x-coordinate denotes the mark number of every Z-shaped waveform, and the y-coordinate is the width of each Z-shaped waveform in pixel unit. Fig. 9 shows that most of the Z-shaped waveforms are close in width and they represent the unbroken single aluminum strand. Besides, there are some Z-shaped waveforms that are much larger or much smaller in width than the unbroken single aluminum strand.

Based on above observations, the width of Z-shaped waveforms can be used to distinguish the broken conductor region

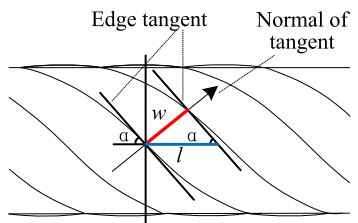


**FIGURE 10.** Schematic diagram of horizontal width of the single aluminum strand.

from the unbroken conductor area. For this reason, it is important to know the horizontal width of a single unbroken aluminum strand, so that the number of broken strands can be further measured.

According to the camera calibration, we can obtain the number of pixels occupied by the diameter of a single aluminum strand, which is represented by  $w$  in Fig. 10. Moreover, it is known that the external aluminum strands are wound in a fixed angle  $α$  (whose minor change is ignored in this paper). Thus, the horizontal width of a single aluminum strand, that is  $l$  in Fig. 10, can be expressed as  $\text{round}(w/\sin \alpha)$ .

On the basis of the above analysis,  $\text{round}(w/\sin \alpha)$  was taken as the reference object, and the appropriate detection accuracy  $v$  which in pixel unit was selected with respect to the actual need.

If the width of a Z-shaped waveform satisfies  $|P_i - \text{round}(w/\sin \alpha)| \leq v$ , where  $P_i$  represents the width of the  $i$ th Z-shaped waveform, then it is identified as the normal waveform representing an unbroken single aluminum strand.

If the width of the Z-shaped waveform meets  $|P_i - \text{round}(w/\sin \alpha)| > v$ , then it is recognized as the abnormal waveform representing the broken aluminum strands.

Furthermore, in order to highlight the width change of the Z-shaped waveforms representing the broken strands, it is necessary to sum the width of adjacent abnormal waveforms. The specific approach is to superpose the width of adjacent abnormal waveforms in Fig. 9. The processing results are shown in Fig. 11, in which the x-coordinate is the mark number of the Z-shaped waveform after superposition, and y-axis represents the width distribution of the Z-shaped waveforms after enhanced processing, the unit is still in pixel.

As shown in Fig. 11, the width superposition results of adjacent abnormal waveforms show obvious peaks, which are consistent with the positions of suspect broken strands, and the more of the broken strands, the larger of its peak value. Moreover, suppose  $H_k$  represents the width of the  $k$ th suspect broken strands region in Fig. 11, the specific width value can be read from y-coordinate of a peak point, and  $l_k$  represents the number of broken aluminum strands based on  $H_k$ , then  $l_k$  can be expressed as  $l_k = \text{round}[H_k / (\text{round}(w/\sin \alpha))]$ , and its maximum value  $l_{\max}$  is the actual number of broken aluminum strands. For example,  $\text{round}(w/\sin \alpha)$  in this paper is about 100 pixels, as shown in Fig. 11(b), there are two peaks

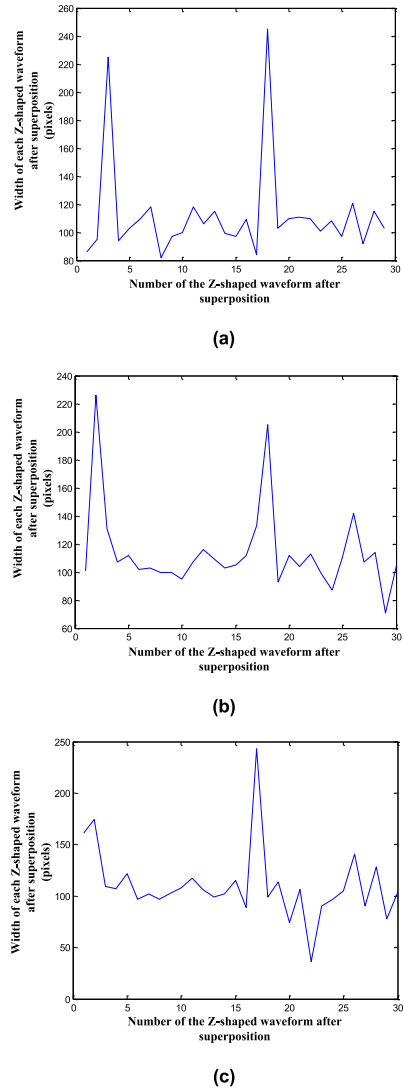


**FIGURE 11.** The superposition results of the Z-shaped waveform of the adjacent broken single aluminum strand. (a) Axis at 1/4 thickness. (b) Central axis. (c) Axis at 3/4 thickness.

representing two positions of suspect broken strands region, and the peak values are about 228 pixels and 200 pixels, so it can be determined that there are two broken aluminum strands respectively at two position on the central axis. Combined with the analysis results at the axes of 1/4 thickness and 3/4 thickness, the positions and numbers of broken strands can be comprehensively determined.

### C. CONDUCTOR DEFECTS IDENTIFICATION

According to the segmentation result of the conductor region obtained in the A part of Section III, the extracted conductor region needs to be mapped to its GVN image, the result is shown in Fig. 12. Comparing Fig. 12(a) and Fig. 12(b), we can observe that surface defects takes higher gray values than other areas in the GVN image of conductor region, furthermore, pixels of a defect are clustered together. As a consequence, the sum of the normalized gray-scale variance value in a column direction will be large if the column crosses

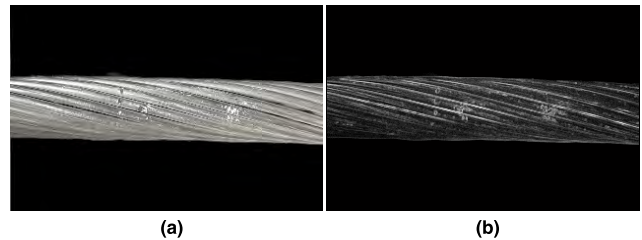


**FIGURE 12.** Images of the conductor region. (a) Extracted conductor region. (b) GVN image of conductor region.

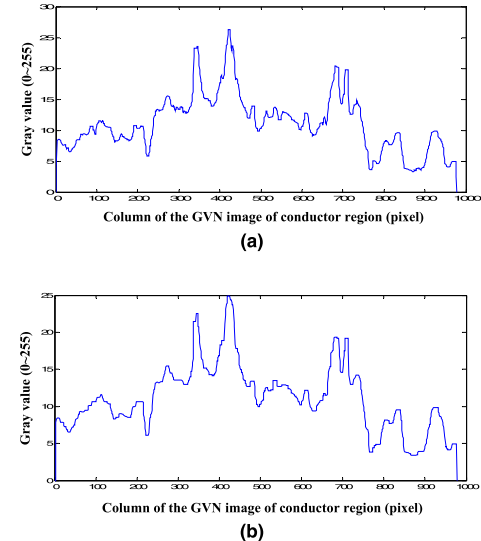


**FIGURE 13.** Processing result of vertical projection. (a) Waveform of vertical projection. (b) Median filtering result of vertical projection.

a defect. Similarly, the sum in a row direction of a local area will also be large if the row passes through a defect. Thereby, we put forward the PGVN algorithm.

The PGVN algorithm includes three main procedures: vertical projection, local horizontal projection, and defects identification. The first procedure analyzes vertical projection of the GVN image of conductor region and locates the horizontal suspect positions of defects. The second step analyzes the horizontal projection of the local subimages obtained by the first procedure. The final procedure identifies every suspect defect position with a rectangle based on the results of the first two procedures and a filtering rule.

#### 1) VERTICAL PROJECTION

Given the GVN image of conductor region in Fig. 12(b), the specific calculation process of its vertical projection is given by

$$m_y = \sum_x F(x, y) \quad (5)$$

where  $F(x, y)$  is the normalized gray-scale variance value at the coordinate  $(x, y)$ ,  $m_y$  represents the summation of  $F(x, y)$  in each column.

The result of the vertical projection is shown in Fig. 13(a), which includes many local peaks. Small local peak is mostly

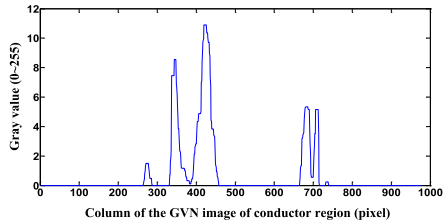
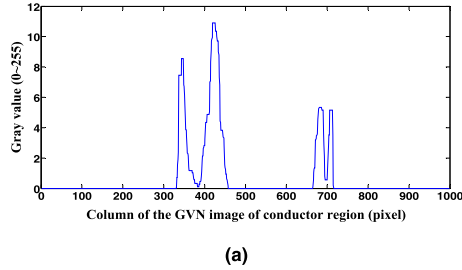


FIGURE 14. Threshold processing results.



(a)

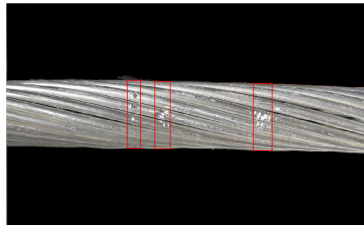
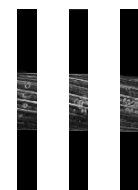
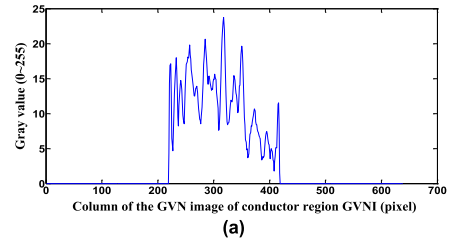
(b)  
(c)

FIGURE 15. Acquisition of the horizontal suspect defects on the conductor. (a) High-pass filtering result. (b) Horizontal suspect defects identification. (c) Local subimages containing suspect defects.

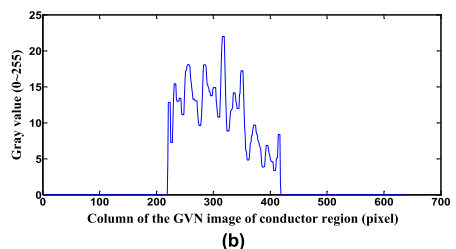
caused by noise and is needed to be smoothed by the median filtering [37]. Fig. 13(b) shows the smoothed result of Fig. 13(a). Note that the horizontal axis refers to each column of the given image, and vertical axis represents the gray value.

In order to highlight the suspect positions of defects, it is necessary to process the results of vertical projection by thresholding, in which the threshold  $T$  is set as mean of the maximum and minimum gray values in the vertical projection, it is expressed as  $T = (M_{\max} + M'_{\min})/2$ . If  $m_y$  is large than  $T$ , then it is set to the difference from the threshold  $T$ . Otherwise, it is set to zero. Fig. 14 shows the threshold processing results.

Furthermore, the threshold result in Fig. 14 needs to be filtered by a high-pass filter, and the size of the filter window is set as the radius  $r$  of a single aluminum strand. If the



(a)



(b)

FIGURE 16. Processing result of vertical projection. (a) Waveform of horizontal projection. (b) Median filtering result of horizontal projection.

pixel range of a peak on the horizontal axis is less than  $r$ , then it is filtered out. Otherwise, it keeps the original value. Fig. 15(a) shows the filtered result, and Fig. 15(b) shows the corresponding horizontal suspect positions of defects. The start column and the end column of the suspect defects region are corresponding to the horizontal coordinate of the high-pass filtered result. Finally, the local subimages containing the suspect defects are shown in Fig. 15(c).

## 2) LOCAL HORIZONTAL PROJECTION

Local horizontal projection is similar to the vertical projection, except that the horizontal projection is carried out by analyzing the sum of the normalized gray-scale variance values of each row in a local sub-image determined by above vertical projection.

First, taking one of the local subimages in Fig. 15(c) as an example, the specific calculation process of its horizontal projection is given by

$$m_x = \sum_y F(x, y) \quad (6)$$

where  $F(x, y)$  is the normalized gray-scale variance value at the coordinate  $(x, y)$ ,  $m_x$  represents the summation of the  $F(x, y)$  in each row.  $m_x$  is also smoothed by median filtering. The result is separately shown in Fig. 16(a) and Fig. 16(b). Note that the horizontal axis refers to each row of the given image, and vertical axis represents the gray value.

Second,  $m_x$  is sequentially processed by thresholding, high-pass filtering and defects marking, just as  $m_y$ . Fig. 17 and Fig. 18 show the corresponding results. Finally, the start row and the end row of the suspect defects are obtained according to the corresponding horizontal coordinate of the high-pass filtered result.

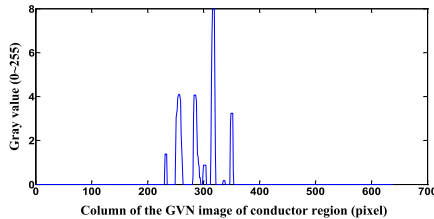


FIGURE 17. Threshold processing results.

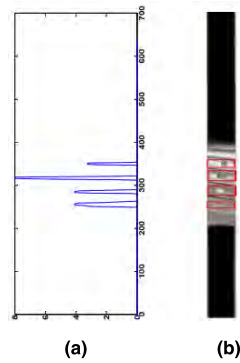


FIGURE 18. Acquisition of the vertical suspect defects on the conductor. (a) High-pass filtering result. (b) Vertical suspect defects identification.

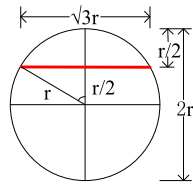


FIGURE 19. Cross-section view of the single aluminum strand.

### 3) DEFECTS IDENTIFICATION

According to the transmission line operation specification [38], the running transmission line is required to be repaired if the defect depth is more than one quarter of the thickness of the single aluminum strand. Therefore, the diameter length at a quarter of the thickness of the single aluminum strand is used as a threshold, which is  $\sqrt{3}r$ , as shown in Fig. 19. And take the specific structural model of the transmission line into account, which is shown in Fig. 20, suppose  $\alpha$  is the angle between the edge tangent of a single aluminum strand and the horizontal line. In order to further screen the obtained suspect defects, we intend to compare the length  $p$  of the suspect defect region with the diameter length  $\sqrt{3}r$ . Note that the length  $p$  is defined as the length that along the normal direction of the conductor edge tangent. If the length  $p$  of the suspect defect region satisfied  $p < \sqrt{3}r$ , then it is ignored. Otherwise, if  $p \geq \sqrt{3}r$ , it is identified and marked.

Based on the technical guidelines for the evaluation of the operation status of overhead transmission lines [39], it is meaningful to make further judgments on the obtained suspect defects. Thereby, the accurate defects position

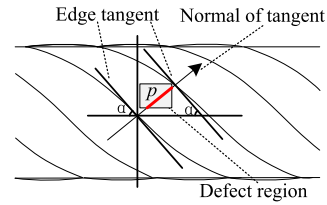


FIGURE 20. Model diagram of transmission line conductor.



FIGURE 21. Identification result of the damage area.



FIGURE 22. UAV and On-site aerial images. (a) UAV equipped with camera. (b) On-site aerial photography.

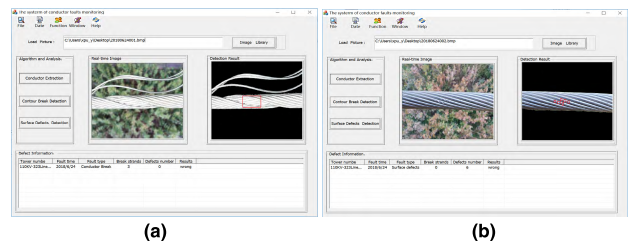


FIGURE 23. The conductor faults analysis software interface. (a) Conductor break detection. (b) Conductor surface defects detection.

is located, Fig. 21 shows the final defects identification results.

## IV. FIELD EXPERIMENTAL RESULTS AND ANALYSIS

In this section, we mainly analyze the performance of the conductor break detection algorithm and the conductor surface defects identification algorithm. All images used in this experiment are obtained by aerial photography in actual transmission lines.

### A. FIELD INSTALLATION

As shown in Fig. 22, the image acquisition device is installed on the UAV, which has already been widely applied in daily patrol of many overhead transmission lines.

Fig. 23 shows that the conductor faults analysis software which is installed in the monitoring center. This software contains several function modules, such as image reading, conductor extraction, conductor break detection, and conductor surface defects detection, etc. The UAV

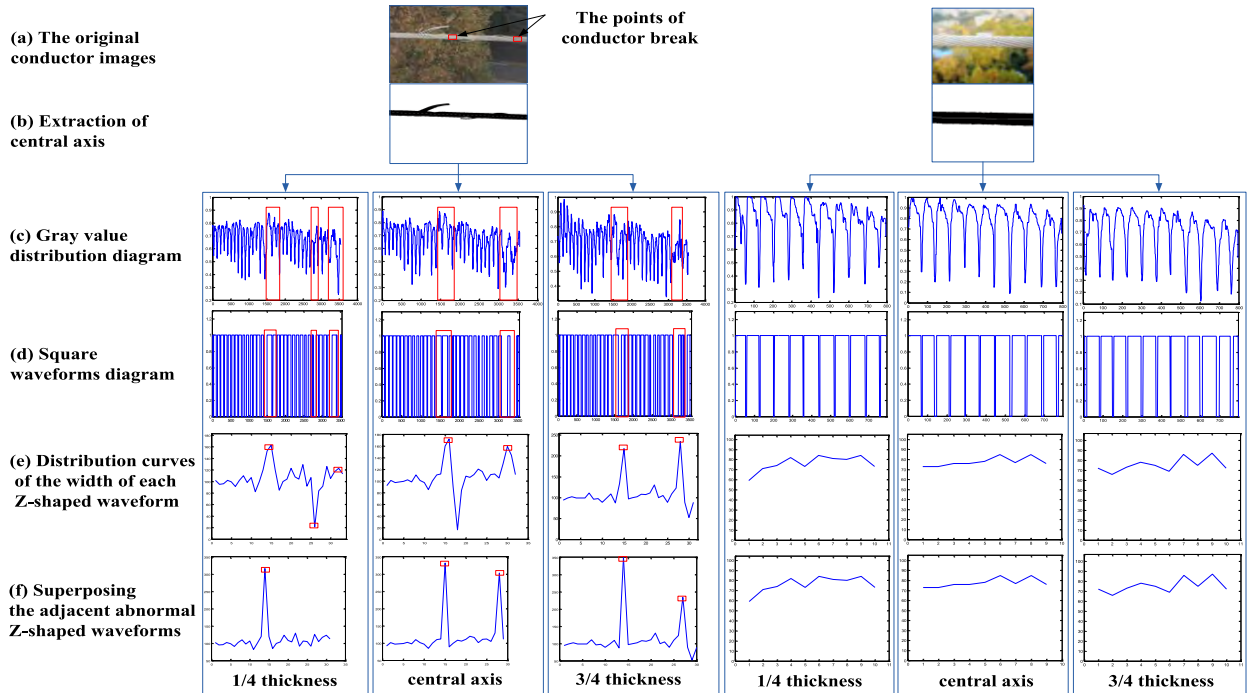


**FIGURE 24.** The flow chart of the conductor break detection. (a) The original conductor images. (b) Extraction of central axis. (c) Gray value distribution diagram. (d) Square waveforms diagram. (e) Distribution curves of the width of each Z-shaped waveform. (f) Superimposing the irregular Z-shaped waveforms.

is required to be as close as possible to the transmission lines so that the mounted camera can capture high-definition conductor images. Therefore, the flight path of the UAV, the fixed-point photographic angle and the communication networks should be set properly according to the requirements [40].

## B. PERFORMANCE TEST OF CONDUCTOR BREAK DETECTION ALGORITHM

### 1) VERIFICATION OF ALGORITHM

In order to systematically verify the validity and practicability of the conductor break detection algorithm proposed in this paper, we take two pictures of filed images as examples for processing and analysis, one is the image of damaged conductor with three broken aluminum strands, and the other one is the unbroken conductor image. The flow chart of the detection process is shown in Fig. 24 below.

The original images are shown in Fig. 24(a). Fig. 24(b) is the central axis extraction results of the conductor region for each image. Fig. 24(c) shows the gray value distribution diagram on three transverse axes of the conductor. We can observe that the gray value distribution on the unbroken conductor axis has a perfect periodic cycle characteristic. As for the broken conductor, the gray value still shows a certain periodic distribution if the axis crosses the undamaged portion, while the periodic gray distribution is destroyed if the axis passes through the broken aluminum strands area. Fig. 24 (d) shows the results of SWT, it is obvious that the Z-shaped waveforms of the unbroken conductor image have nearly the same width with each other, while the Z-shaped

waveforms corresponding to the broken aluminum strands portion has a local sudden increase or continuous decrease in width. This phenomenon is clearer in the statistical distribution of the width of the Z-shaped waveforms on each axis shown in Fig. 24(e). Fig. 24(f) shows the width superposition results of the adjacent abnormal Z-shaped waveforms. The locations of the broken aluminum strands on the whole conductor is clear at a glance in Fig. 24(f). The maximum value in the result of the Z-shaped waveform width superposition tell us there are three broken aluminum strands in the broken conductor, which is consistent with the actual situation.

### 2) DIFFERENT BACKGROUND

In addition, the performance of the proposed conductor breakage detection algorithm is further evaluated based on several filed images captured by UAV under simple backgrounds and complex backgrounds. The experimental results under different backgrounds are provided in Table 3, including the results of key intermediate processes. It is demonstrated that the proposed algorithm performs well under different conditions and can obtain robust detection and diagnosis results.

### 3) FIELD DATA SET VERIFICATION

As shown in Table 4, a data set with 400 filed images under simple backgrounds and 400 filed images under complex backgrounds captured by UAV are constructed to verify the effectiveness and robustness of the conductor break detection algorithm. As the results shows that the detection accuracy

**TABLE 3.** Experimental results under different backgrounds.

Number	1	2	3	4	5	6
Image						
GVN image of conductor region						
Superposition results on central axis						
Detected conductor break						
Detected broken strands	1	2	2	2	1	5
Actual broken strands	1	2	2	2	1	5

**TABLE 4.** Recognition results of conductor break.

Simple backgrounds				
Total images	100	100	100	100
Actual broken strands images	55	55	55	55
Accurate recognition Accuracy	53	54	52	51
	96.36%	98.18%	94.55%	92.73%
Complex backgrounds				
Total images	100	100	100	100
Actual broken strands images	55	55	55	55
Accurate recognition Accuracy	50	47	46	45
	90.91%	85.45%	83.64%	81.82%

in simple condition is higher than that in complex condition and the average detection accuracy can reach 90.45%, which can effectively detect the conductor break in the transmission line.

### C. PERFORMANCE TEST OF CONDUCTOR SURFACE DEFECTS DETECTION ALGORITHM

#### 1) VERTIFICATION OF ALGORITHM

In order to verify the effectiveness and practicability of the conductor surface defects identification algorithm proposed in this paper, a filed image containing several surface defects is chosen as an example. The flow chart of the detection process is shown in Fig. 25 below.

It can be seen from Fig. 25(a) that the suspect column containing defects on the horizontal direction can be effectively highlighted by the vertical projection and high-pass filtering of the GVN image of the conductor region, which effectively reduce the detection range of the suspect conductor defects region, and then three sub-images containing the defects are obtained by column segmentation. Thereafter, as shown in Fig. 25(b), as same as the vertical projection, the local horizontal projection of each subimage is first calculated separately, and each projection result is successively processed by the median filtering, threshold processing, and high-pass filtering. Followed by the row segmentation on each subimage, the position of suspect defects can be localized and identified. Finally, according to the screening principle, the small interference area is filter out, the final results are shown in Fig. 25(c).

#### 2) DIFFERENT BACKGROUND

Similarly, the performance of the proposed conductor defects detection algorithm is also evaluated based on several aerial images under simple backgrounds and complex backgrounds. The experimental results are provided in Table 5, including the results of key intermediate processes. It is demonstrated that the proposed algorithm performs well under different conditions and can obtain robust detection and diagnosis results.

#### 3) FIELD DATA SET VERIFICATION

As the same, in order to verify the effectiveness and robustness of the conductor defects detection algorithm, a data set with 400 aerial images under simple backgrounds and 400 aerial images under complex backgrounds are con-

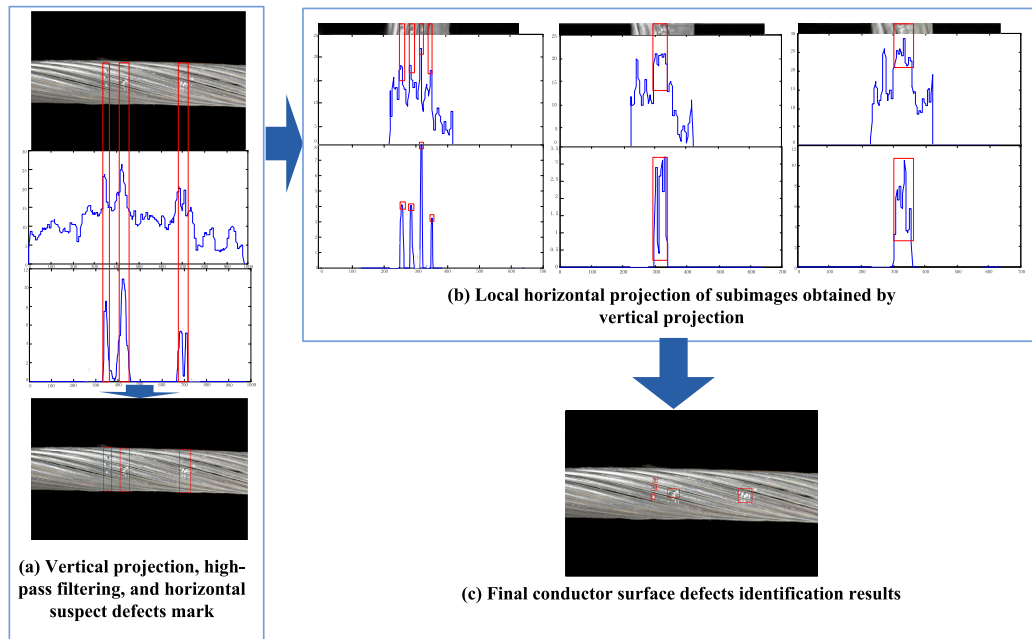


**FIGURE 25.** The flow chart of the conductor defects detection. (a) Vertical projection, high-pass filtering, and horizontal suspected defects mark. (b) Local horizontal projection of sub-images obtained vertical projection. (c) Final conductor surface defects identification results.

**TABLE 5.** Experimental results under different backgrounds.

Number	1	2	3	4	5	6
Image						
GVN image of conductor region						
Vertical projection						
Horizontal suspect defects						
Local horizontal projection						
Suspect defects localization						

structed in the same way. The experiment results in Table 6 shows that the detection accuracy in simple condition is higher than that in complex condition and the average

detection accuracy can reach 92.05%, which can effectively detect the conductor surface defects in the transmission line.

**TABLE 6.** Recognition results of conductor defects.

Simple backgrounds				
Total images	100	100	100	100
Actual defects images	55	55	55	55
Accurate identification	54	54	52	53
Accuracy	98.18%	98.18%	94.55%	93.36%
Complex backgrounds				
Total images	100	100	100	100
Actual defects images	55	55	55	55
Accurate identification	49	46	50	47
Accuracy	89.91%	83.64%	90.91%	85.45%

## V. CONCLUSION AND FUTURE WORK

In this paper, a recognition technology for transmission lines conductor break and surface damage detection based on aerial images is proposed. The proposed GVN enhancement processing method can highlight the conductor from UAV captured aerial images with different background, which further promotes the subsequent conductor region segmentation. Afterward, the conductor break can be identified and located by analyze the gray value distribution on the GVN image of conductor region. Meanwhile, the conductor surface defects can also be identified and located by the vertical projection and horizontal projection on the GVN image of conductor region. The performance of the proposed algorithms is extensively evaluated for a range of different backgrounds. The field experimental results confirm its effectiveness and robustness as well as its practicability. The average fault detection accuracy for conductor break identification can reach 90.45%, while the average fault detection accuracy for conductor surface defects identification can reach 92.05%. As a result, the proposed technology can be adopted in the UAV patrol inspection system of transmission lines.

The proposed technology is able to locate the conductor break and conductor surface defects on the acquired aerial images, but the specific positions of the faults in the whole transmission line is not implemented. Also, the faults types cannot be automatically differentiated during the fault detection process in the proposed technology. Therefore, a number of research directions are considered worth further research effort. Firstly, more advanced approach is needed to efficiently distinguish different types of faults for better state assessment of transmission lines. Secondly, with the development of panoramic image acquisition technology, the specific positions of the faults in the whole line can be obtained based on the camera calibration. Finally, additional work is needed for location and detection of other faults on conductors by combining the image processing technology with the sensor technology which is immune to complex field environment and illumination.

## REFERENCES

- [1] J. Qiao, J. Zou, J. Zhang, Y. Lu, J. Lee, and M.-N. Ju, "Space-time pattern of ion flow under AC/DC hybrid overhead lines and its application," *IEEE Trans. Power Del.*, vol. 33, no. 5, pp. 2226–2235, Oct. 2018.
- [2] Y. Huangfu, L. D. Rienzo, and S. Wang, "Frequency-dependent multi-conductor transmission line model for shielded power cables considering geometrical dissymmetry," *IEEE Trans. Magn.*, vol. 54, no. 3, Mar. 2017, Art. no. 6300104.
- [3] P. Nichols and T. J. Summers, "Evaluation of length, dependent Earth return transmission-line parameters for overhead conductors in the quasistatic range," *IEEE Trans. Power Del.*, vol. 33, no. 4, pp. 1589–1598, Aug. 2018.
- [4] D. H. Waters, J. Hoffman, E. Hakansson, and M. Kumosa, "Low-velocity impact to transmission line conductors," *Int. J. Impact Eng.*, vol. 106, pp. 64–72, Aug. 2017.
- [5] C. Rakpenthai and S. Uatrongjit, "Power system state and transmission line conductor temperature estimation," *IEEE Trans. Power Syst.*, vol. 32, no. 3, pp. 1818–1827, May 2017.
- [6] A. A. M. Farah, M. M. Afonso, J. A. Vasconcelos, and M. A. O. Schroeder, "A finite-element approach for electric field computation at the surface of overhead transmission line conductors," *IEEE Trans. Magn.*, vol. 54, no. 3, Mar. 2018, Art. no. 7400904.
- [7] S. M. H. Hosseini and P. R. Baravati, "New high frequency multi-conductor transmission line detailed model of transformer winding for PD study," *IEEE Trans. Dielectr. Electr. Insul.*, vol. 24, no. 1, pp. 316–323, Feb. 2017.
- [8] C. G. de Carvalho, C. E. M. Costa, S. Kurokawa, and J. Pissolato, "Alternative phase-domain model for multi-conductor transmission lines using two modal transformation matrices," *Electr. Power Compon. Syst.*, vol. 44, no. 3, pp. 291–301, Feb. 2016.
- [9] J. Zhang, L. Liu, B. Wang, X. Chen, Q. Wang, and T. Zheng, "High speed automatic power line detection and tracking for a UAV-based inspection," in *Proc. ICICEE*, Xi'an, China, Aug. 2012, pp. 266–269.
- [10] Y. Wu, Y. Sui, and G. Wang, "Vision-based real-time aerial object localization and tracking for UAV sensing system," *IEEE Access*, vol. 5, pp. 23969–23978, 2017.
- [11] Y. Zhang, X. Yuan, W. Li, and S. Chen, "Automatic power line inspection using UAV images," *Remote Sens.*, vol. 9, no. 8, p. 824, Aug. 2017.
- [12] V. N. Nguyen, R. Jenssen, and D. Roverso, "Automatic autonomous vision-based power line inspection: A review of current status and the potential role of deep learning," *Int. J. Electr. Power Energy Syst.*, vol. 99, pp. 107–120, Jul. 2018.
- [13] B. Li and C. Chen, "Transmission line detection based on a hierarchical and contextual model for aerial images," *Proc. SPIE*, vol. 27, no. 4, Jul. 2018, Art. no. 03054.
- [14] G. Yan, C. Li, G. Zhou, W. Zhang, and X. Li, "Automatic extraction of power lines from aerial images," *IEEE Geosci. Remote Sens. Lett.*, vol. 4, no. 3, pp. 387–391, Jul. 2007.
- [15] Z. Li, Y. Liu, R. Walker, R. Hayward, and J. Zhang, "Towards automatic power line detection for a UAV surveillance system using pulse coupled neural filter and an improved Hough transform," *Mach. Vis. Appl.*, vol. 21, no. 5, pp. 677–686, Aug. 2010.
- [16] A. Zhao, X. Bi, J. Hui, C. Zeng, and L. Ma, "An improved aerial target localization method with a single vector sensor," *Sensors*, vol. 17, no. 11, p. 2619, Nov. 2017.
- [17] Q. Wu, J. An, and B. Lin, "A texture segmentation algorithm based on PCA and global minimization active contour model for aerial insulator images," *IEEE J. Sel. Topics Appl. Earth Observ. Remote Sens.*, vol. 5, no. 5, pp. 1509–1518, Oct. 2012.
- [18] X. Huang, H. Zhang, and Y. Zhang, "Automatic identification and location technology of glass insulator self-shattering," *Proc. SPIE*, vol. 26, no. 6, Nov. 2017, Art. no. 063014.
- [19] Y. Zhai, R. Chen, Q. Yang, X. Li, and Z. Zhao, "Insulator fault detection based on spatial morphological features of aerial images," *IEEE Access*, vol. 6, pp. 35316–35326, 2018.
- [20] X. Miao, X. Liu, J. Chen, S. Zhuang, J. Fan, and H. Jiang, "Insulator detection in aerial images for transmission line inspection using single shot multibox detector," *IEEE Access*, vol. 7, pp. 9945–9956, 2019.
- [21] R. Z. Homma, O. Aohn, and R. C. Bose, "Analysis of the recognition and localisation techniques of power transmission lines components in images acquired by drones," in *Proc. 24th CIRED*, Glasgow, U.K., Jun. 2017, vol. 2017, no. 1, pp. 29–32.

- [22] J. Lu *et al.*, "Detection of bird's nest in high power lines in the vicinity of remote campus based on combination features and cascade classifier," *IEEE Access*, vol. 6, pp. 39063–39071, 2018.
- [23] Y. Li, Y. F. Li, Q. L. Wang, D. Xu, and M. Tan, "Measurement and defect detection of the weld bead based on online vision inspection," *IEEE Trans. Instrum. Meas.*, vol. 59, no. 7, pp. 1841–1849, Jul. 2010.
- [24] A. Valla and F. Molinari, "A vision-based technique for lay length measurement of metallic wire ropes," *IEEE Trans. Instrum. Meas.*, vol. 58, no. 5, pp. 1756–1762, May 2009.
- [25] Q. Li and S. Ren, "A real-time visual inspection system for discrete surface defects of rail heads," *IEEE Trans. Instrum. Meas.*, vol. 61, no. 8, pp. 2189–2199, Aug. 2012.
- [26] L. A. Elrefaei, A. Bajaber, S. Natheirm, N. AbuSanab, and M. Bazi, "Automatic electricity meter reading based on image processing," in *Proc. IEEE Jordan Conf. Appl. Electr. Eng. Comput. Technol. (AEECT)*, Amman, Jordan, Nov. 2015, pp. 1–5.
- [27] A. Anis, M. Khaliluzzaman, M. Yakub, N. Chakraborty, and K. Deb, "Digital electric meter reading recognition based on horizontal and vertical binary pattern," in *Proc. 3rd Int. Conf. Electr. Inf. Commun. Technol. (EICT)*, Khulna, Bangladesh, Dec. 2017, pp. 1–6.
- [28] S. Shirmohammadi and A. Ferrero, "Camera as the instrument: The rising trend of vision based measurement," *IEEE Trans. Instrum. Meas.*, vol. 17, no. 3, pp. 41–47, Jun. 2014.
- [29] R. G. Lins, S. N. Givigi, and P. R. G. Kurka, "Vision-based measurement for localization of objects in 3-D for robotic applications," *IEEE Trans. Instrum. Meas.*, vol. 64, no. 11, pp. 2950–2958, Nov. 2015.
- [30] R. Z. Homma, C. Szymanski, and R. A. Faraco, "Information and communication architecture for transmission power line inspections using unmanned aircraft system," in *Proc. 24th CIRED*, Glasgow, U.K., Jun. 2017, vol. 2017, no. 1, pp. 238–241.
- [31] M. Lu, M. Bagheri, A. P. James, and T. Phung, "Wireless charging techniques for UAVs: A review, reconceptualization, and extension," *IEEE Access*, vol. 6, pp. 29865–29884, 2018. doi: [10.1109/ACCESS.2018.2841376](https://doi.org/10.1109/ACCESS.2018.2841376).
- [32] R. Z. Homma, A. Cesentino, and C. Szymanski, "Autonomous inspection in transmission and distribution power lines—Methodology for image acquisition by means of unmanned aircraft system and its treatment and storage," in *Proc. 24th CIRED*, Glasgow, U.K., Jun. 2017, vol. 2017, no. 1, pp. 965–967.
- [33] J. T. Dong and J. Wang, "Comparison of three image processing methods realized by VC++ calling MATLAB," *Mod. Electron. Techn.*, vol. 35, no. 16, pp. 46–49, Aug. 2012.
- [34] J. L. Li, W. Z. Zhang, H. F. Ma, and X. Liu, "Research on license plate recognition technology based on HALCON," *J. Northwest Normal Univ. (Natural Sci.)*, vol. 51, no. 6, pp. 54–57, 2015.
- [35] X. Huang, F. Zhang, H. Li, and X. Liu, "An online technology for measuring icing shape on conductor based on vision and force sensors," *IEEE Trans. Instrum. Meas.*, vol. 66, no. 12, pp. 3180–3189, Dec. 2017.
- [36] X. Huang, L. Yang, Y. Zhang, Y. Zhu, and G. Zhang, "A measurement technology of space distance among transmission bundle conductors based on image sensors," *IEEE Trans. Instrum. Meas.*, to be published. doi: [10.1109/TIM.2018.2885265](https://doi.org/10.1109/TIM.2018.2885265).
- [37] Y. Xia, X. Jiang, Z. Zhang, J. Hu, and C. Sun, "Detecting broken strands in transmission line—Part 1: Design of a smart eddy current transducer carried by inspection robot," *Int. Trans. Electr. Energy Syst.*, vol. 23, no. 8, pp. 1409–1422, Nov. 2012.
- [38] *Operating Regulations for Overhead Transmission Lines*, document DL/T 741-2010, 2010.
- [39] *Technical Guidelines for Operational State Assessment of Overhead Transmission Lines*, document DL/T 1249-2013, 2013.
- [40] O. Menéndez, M. Pérez, and F. A. Cheein, "Visual-based positioning of aerial maintenance platforms on overhead transmission lines," *Appl. Sci.*, vol. 9, no. 1, p. 165, Jan. 2019.



**YE ZHANG** received the B.S. and M.S. degrees in electronic information engineering from Xi'an Polytechnic University, Xi'an, China, in 2011 and 2014, respectively. She is currently pursuing the Ph.D. degree in mechanical and electronic engineering with the School of Mechano-Electronic Engineering, Xidian University.



**XINBO HUANG** received the B.S. and M.S. degrees in automation from Qingdao Technological University, Qingdao, China, in 1998 and 2001, respectively, and the Ph.D. degree in automation from Xidian University, Xi'an, China, in 2005. He is currently a Professor with the School of Electronics Information, Xi'an Polytechnic University, Xi'an, and also a Ph.D. Supervisor with the School of Electro-Mechanical Engineering, Xidian University. His current research interests include online monitoring technology, image recognition technology, and wireless network sensors.



**JIANYUAN JIA** received the M.S. degree from Xidian University, Xi'an, China, in 1981, where he is currently a Professor and a Ph.D. Supervisor with the School of Electro-Mechanical Engineering. His research interests include the design and theory of micro-electromechanical systems, the technology of protecting electronic equipment against harsh environment, and the development of electromechanical control systems and device.



**XINHUI LIU** received the B.S. and M.S. degrees in electronic information engineering from Xi'an Polytechnic University, Xi'an, China, in 2015 and 2018, respectively. She is currently pursuing the Ph.D. degree in computer science and technology with Xi'an Jiaotong University. Her research interests include the applications in deep learning and artificial intelligence.